ISSN 0965-5425, Computational Mathematics and Mathematical Physics, 2022, Vol. 62, No. 8, pp. 1331–1344. © Pleiades Publishing, Ltd., 2022.
Russian Text © The Author(s), 2022, published in Zhurnal Vychislitel'noi Matematiki i Matematicheskoi Fiziki, 2022, Vol. 62, No. 8, pp. 1360–1373.

PARTIAL DIFFERENTIAL EQUATIONS

Detecting Two-Dimensional Fingering Patterns in a Non-Equilibrium PDE Model via Adaptive Moving Meshes

P. A. Zegeling[a]

[a] *Utrecht University, Utrecht, The Netherlands*

e-mail: P.A.Zegeling@uu.nl

Received October 10, 2021; revised March 3, 2022; accepted April 11, 2022

Abstract—This article discusses an adaptive mesh method applied to a bifurcation problem in a non-equilibrium Richard's equation from hydrology. The extension of this PDE model for the water saturation S, to take into account additional dynamic memory effects gives rise to an extra third-order mixed space-time derivative term in the PDE. The one-space dimensional case predicts the formation of steep non-monotone waves depending on the non-equilibrium parameter. In two space dimensions, this parameter and the frequency in a small perturbation term, predict that the waves may become *unstable*, thereby initiating so-called gravity-driven fingers. To detect the steep solutions of the time-dependent PDE model, we have used a sophisticated adaptive moving mesh method based on a scaled monitor function.

Keywords: traveling waves, (non-)monotonicity, porous media, fingering structures, adaptive moving mesh

DOI: 10.1134/S0965542522080140

1. INTRODUCTION

This article discusses the importance of both the analysis and computation in relation to a bifurcation problem in a non-equilibrium Richard's equation from hydrology. The extension of this PDE model for the water saturation, to take into account additional dynamic memory effects, was suggested by Hassanizadeh and Gray [1] at the end of the last century. This gives rise to an extra third-order mixed space-time derivative term in the PDE. In one space dimension, travelling wave analysis predicts the formation of steep non-monotone waves depending on the non-equilibrium parameter. It is shown that, in this framework, theory from applied analysis, accurate numerical PDE solutions and also the experimental observations from the laboratory [2, 3] can be nicely matched. In two space dimensions, the non-equilibrium parameter τ and the frequency (appearing in a small perturbation term), predict that the waves may become *unstable*, thereby initiating so-called gravity-driven fingers. This phenomenon can be analysed with a linear stability analysis is confirmed by the numerical experiments of the 2D time-dependent PDE model. For this purpose, we have used an efficient adaptive moving mesh technique based on a scaled monitor function. The numerical experiments in one and two space dimensions confirm the theoretical predictions and show the effectiveness of the adaptive mesh solver.

2. THE NON-EQUILIBRIUM PDE MODEL

The two-dimensional PDE model describing the non-equilibrium effects in a two-phase porous medium is described by [1, 4–8]:

$$\begin{aligned} S_t &= \nabla \cdot (\mathscr{D}(S)\nabla S) + [f(S)]_z + \tau \nabla \cdot [f(S)\nabla(S_t)], \\ &\text{with} \quad (x,z,t) \in [x_L, x_R] \times [z_L, z_R] \times (0,T], \end{aligned} \tag{1}$$

where S is the water saturation, τ is the non-equilibrium parameter, $D(S)$ is a nonlinear diffusion function and $f(S)$ is a so-called fractional flow function, respectively.

2.1. The One-Dimensional Case

First, let us take a brief look at the one-dimensional case. For this, assuming a constant diffusion and a linearized non-equilibrium term, PDE model (1) can be simplified to:

$$S_t = \mathcal{D}\, S_{zz} + [f(S)]_z + \tau S_{zzt}, \quad (z,t) \in [z_L, z_R] \times (0,T], \tag{2}$$

with initial condition $S(z,0) = S_0(z)$.

The water saturation in one space dimension is represented by the variable $S(z,t) \in [0,1]$, $\mathcal{D} > 0$ is a diffusion coefficient and $\tau \geq 0$ the non-equilibrium parameter (see also [1, 5, 6]). The function f satisfies:

$$f(0) = 0, \quad f(1) = 1, \quad f'(S) > 0$$

and is related to a fractional flow function in the porous media model [5]. In particular, two choices for the function f are considered. The first one is a convex-shaped function, representing a one phase situation (only water), i.e.,

$$f(S) = \frac{S^2}{2},$$

and the second one is a convex-concave function, indicating two phases (both water and air are present):

$$f(S) = \frac{S^2}{S^2 + (1-S)^2}.$$

Dirichlet conditions are imposed at the spatial boundaries:

$$S(z_L,t) = S_- \quad \text{and} \quad S(z_R,t) = S_+.$$

The initial water saturation $S_0(z)$, the boundaries of the spatial domain, the final time T and the values for $0 \leq S_- < S_+ \leq 1$, $\mathcal{D}$ and τ will be specified in the description of the numerical experiments.

2.2. A Bifurcation Diagram and Travelling Waves

This short section discusses solutions of PDE model (2) in the form of travelling waves (TWs). For simplicity, assume now that $f(S) = S^2$. The convex-concave case is treated in [5, 6] which gives rise to an even richer structure of the dynamics (see Fig. 1). The TW ansatz, assuming a positive constant speed c, can be written as:

$$S(z,t) = \varphi(z + ct) := \varphi(\eta), \quad \eta \in (-\infty, +\infty), \quad c > 0.$$

Substituting this ansatz in PDE (2), yields the third-order ODE:

$$c\varphi' = D\,\varphi'' + [\varphi^2]' + c\tau\varphi''', \tag{3}$$

where the ' stands for taking derivatives with respect to the TW-variable η. Integrating (3) between $-\infty$ and η and using the fact that $\varphi(-\infty) = S_-$, $\varphi'(-\infty) = \varphi''(-\infty) = 0$, gives the folllowing system of first-order ODEs:

$$\begin{aligned} \varphi' &= \psi, \\ \psi' &= \frac{c(\varphi - S_-) + S_-^2 - \varphi^2 - D\,\psi}{c\,\tau}. \end{aligned} \tag{4}$$

A TW for (2) in the original coordinate system (x,t) is represented by a trajectory in the (φ,ψ)-plane connecting an unstable stationary point (at $\eta = -\infty$) of (4) with a stable one (at $\eta = +\infty$). There are only two stationary points in system (4):

$$(\varphi,\psi) = (S_-,0) \quad \text{and} \quad (\varphi,\psi) = (S_+,0).$$

It can be deduced that non-monotone TWs exist for

$$\tau > \tau_c = \frac{\mathcal{D}^2}{S_+ - S_-}.$$

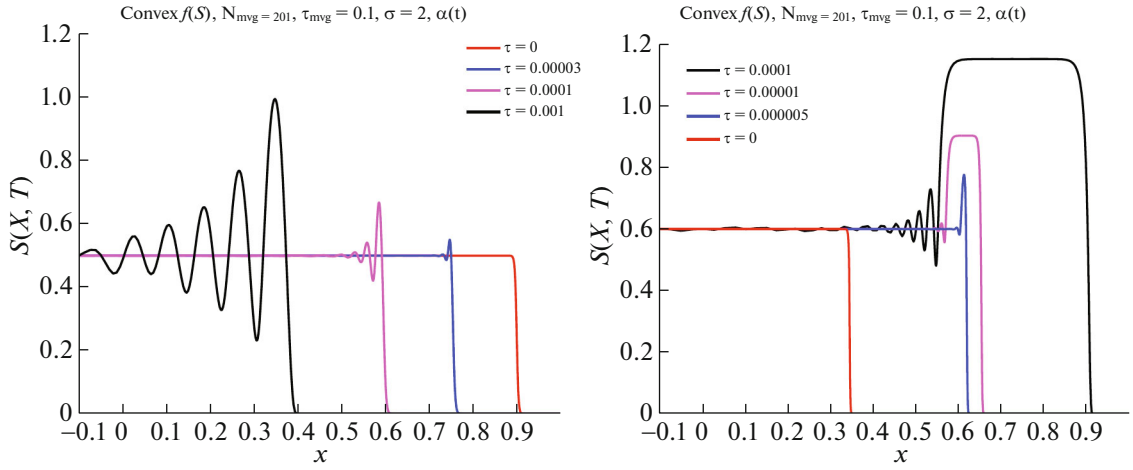

Fig. 1. In the left frame the solutions in one space dimension are shown for a convex fractional flow function, and in the right frame for the convex-concave case for different values of the non-equilibrium parameter $\tau \geq 0$.

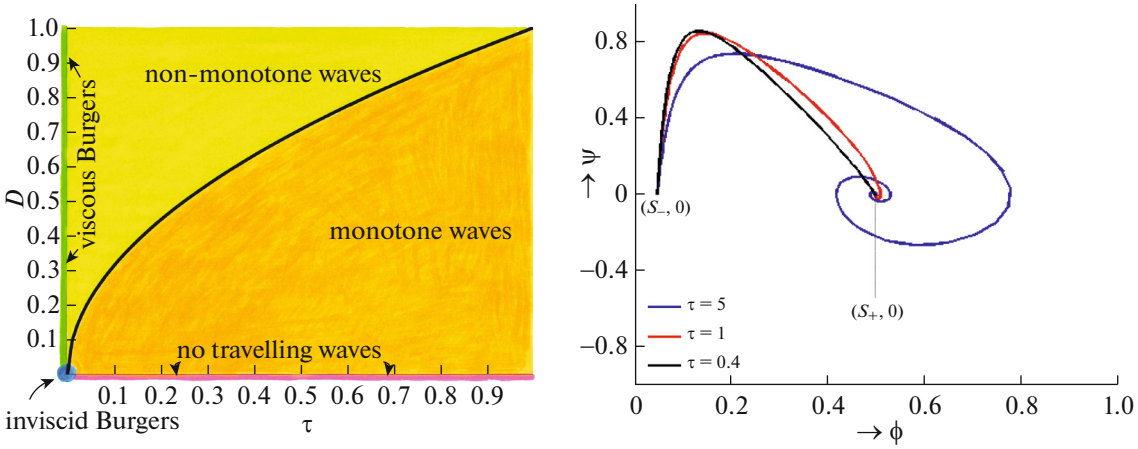

Fig. 2. A bifurcation diagram (left panel) indicating the existence of monotone waves and non-monotone waves depending on the parameters $\mathcal{D}$ and τ. The black curve is defined by: $\mathcal{D} = \sqrt{\tau(S_+ - S_-)}$. The right panel shows, for three different values of the parameter τ, trajectories in the phase plane (φ, ψ). The red and blue curves correspond to non-monotone waves ($\tau > \tau_c > 0$) and the black curve denotes a monotone wave ($\tau = 0$).

This situation is clarified in a bifurcation diagram (left panel in Fig. 2) and a phase plane plot (right panel in Fig. 2). For $\tau = 0$, it is known that only monotone waves satisfy the PDE model [4]. Since we are looking also for non-monotone waves, we need the extra τ-term in PDE (2) to describe such phenomena.

2.3. The One-Dimensional Adaptive Moving Mesh

For the numerical simulations of PDE model (2) in one space dimension, we use an adaptive moving mesh technique based on a general coordinate transformation from (z, t) to (ξ, θ) (for more details: [7, 9–13]) The transformed PDE model in the new variables ξ and θ is coupled with the adaptive mesh PDE:

$$[\sigma(\mathcal{J}) + \tau_s \mathcal{J}_\vartheta) \mathcal{M}]_\xi = 0, \quad \tau_s \geq 0,$$

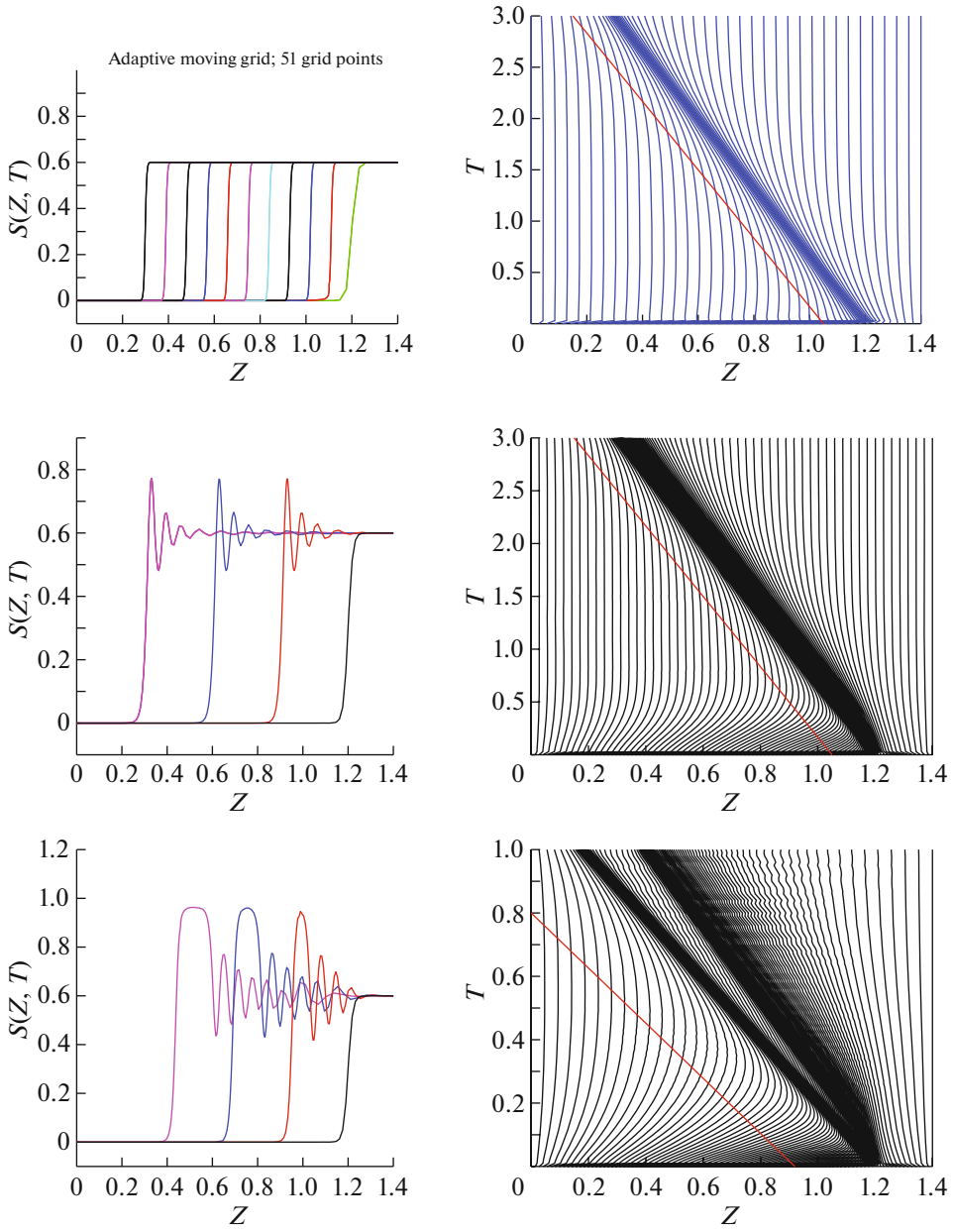

Fig. 3. The time history of the adaptive mesh (the three panels on the right), the solutions at a few points of time (the three left panels) for three characteristic cases in the porous media model: the case $\tau = 0$ (top), a convex f (middle) and a convex-concave f (bottom). The red straight lines indicate the exact (asymptotic) wave speeds for the three cases, as predicted by formula (6).

where $\mathcal{J} = z_\xi$ is the Jacobian of the transformation and

$$\mathcal{M} := \sqrt{1 + [S_z]^2}$$

is the monitor function, reflecting the dependence of the non-uniform mesh on the spatial derivative of the PDE solution.

The operator

$$\sigma := \mathcal{J} + \kappa_s(\kappa_s + 1)\frac{\partial^2}{\partial \xi^2}$$

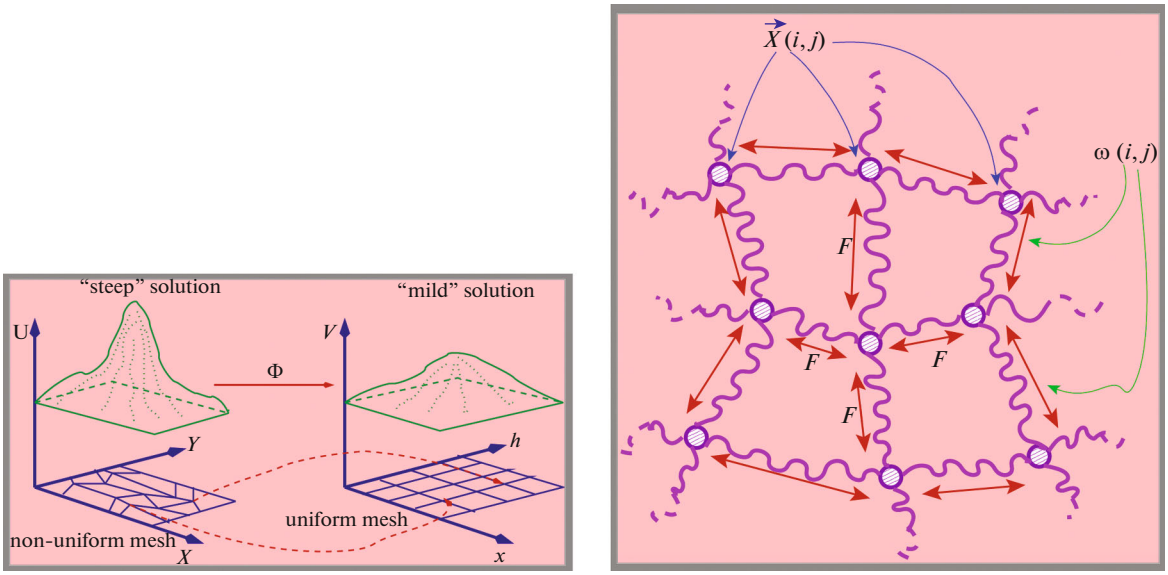

Fig. 4. The two-dimensional mesh transformation. In the left panel we can see how a transformation maps a steep solution into a milder solution; in the right panel the adaptive mesh can be seen as a system of springs with spring forces F located at $\mathbf{x}(i, j)$ in terms of monitor function values ω.

is applied to obtain a smoother mesh transformation in space. The first adaptivity constant, $\kappa_s > 0$ $(= \mathbb{O}(1))$ is a spatial smoothing (or filtering) parameter. The second adaptivity constant τ_s $(= \mathbb{O}(10^{-3}))$ takes care of the smoothness in the time-direction. For $\kappa_s > 0$ and $\tau_s > 0$, after semi-discretization, it can be shown [11] that the spatial non-uniform mesh satisfies the condition:

$$\frac{\kappa_s}{\kappa_s + 1} \leq \frac{\Delta z_{i+1}}{\Delta z_i} \leq \frac{\kappa_s + 1}{\kappa_s}$$

for all meshpoints z_i and all time $t > 0$. Note that, for $\kappa_s = \tau_s = 0$ (no smoothing), we return to the basic equidistribution principle:

$$[z_\xi \mathcal{M}]_\xi = 0.$$

For more details on the adaptive mesh and the smoothing operators we refer to [11–13]. The transformed PDE and the adaptive mesh PDE are simultaneously semi-discretized in the spatial direction following a method-of-lines approach. A central, second-order, uniform approximation for the transformed derivative terms in the ξ-direction is used. The time-integration of the resulting coupled ODE-system is done by a BDF method with variable time-steps in DASSL [14].

2.4. Numerical Results in 1D

In this section, we perform some numerical experiments to illustrate the accuracy and effectiveness of the adaptive moving mesh in one space dimension. This will also confirm the TW analysis in Section 2.2. The adaptive mesh parameters are chosen as follows: $\kappa_s = 2$ and $\tau_s = 0.001$ and the time-integration tolerance in DASSL is set to the value 10^{-4}. The initial condition is a steep wave starting at the right boundary of the domain and reads:

$$S(z,0) = S_0(z) = S_- + \frac{1}{2}(S_+ - S_-)(1 + \tanh(R(z - z_0)), \tag{5}$$

where $z_L = 0$, $z_R = 1.4$, $S_- = 0$, $S_+ = 0.6$, $R = 50$ and PDE parameters: $\tau = 10^{-4}$ and $\mathcal{D} = 10^{-3}$. In Fig. 3 (upper two plots) we show, for $\tau = 0$, in which case we know that only monotone solutions exist, numerical solutions with $N = 51$ adaptive moving mesh points. It is clearly observed that the adaptive mesh

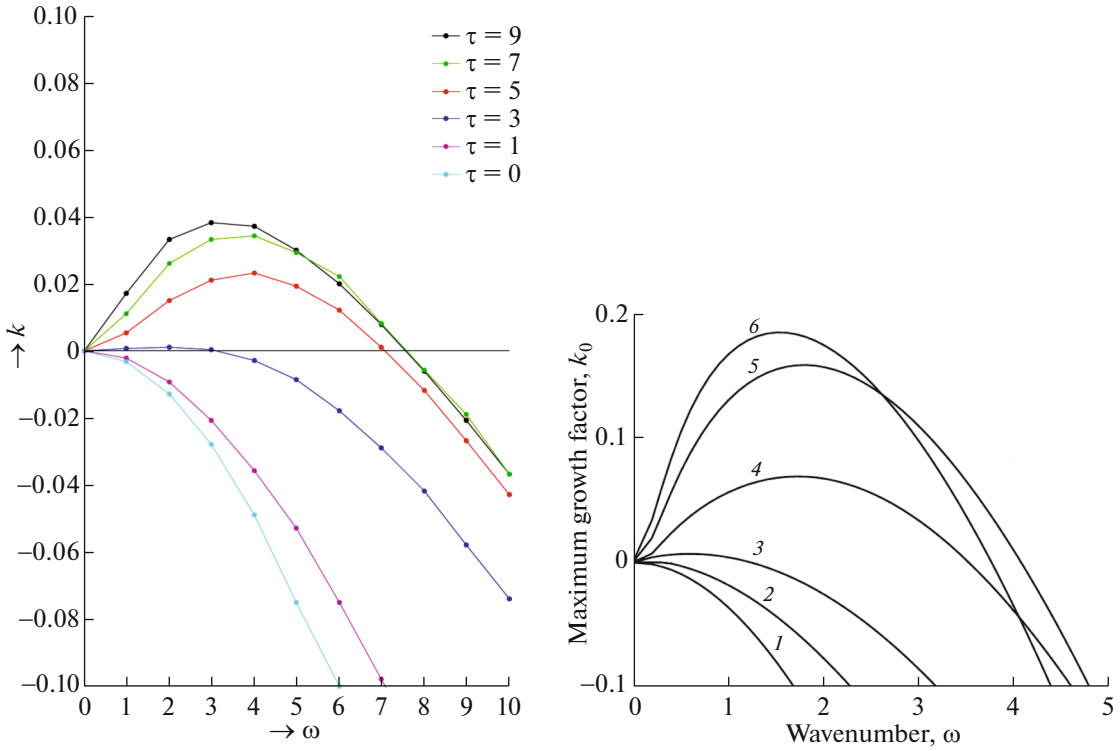

Fig. 5. Left panel: the growth factor k, numerically determined, as a function of the wave number ω of the perturbation for various values of τ; right panel: the theoretical prediction, taken from [15]. Note that the scales on both axes in the two figures are different. The ω (left) is a numerical frequency added to the initial condition, whereas the ω on the right comes from a theoretical analysis. The global behavior is the same, but the exact values are different. A similar remark holds for the growth factor k.

nicely keeps track of the monotone wave. Also, the plot with the time history of the adaptive mesh illustrates the smooth distribution and time-behavior of the mesh with a constant wave velocity. Figure 3 (middle two and lower two plots) displays the difference between the convex and the convex-concave case: non-monotone TWs and plateau-waves.These waves are predicted by the analysis in Section 2.2 and [5].

From ODE system (4) it can easily be derived that the asymptotic travelling-wave speed c satisfies:

$$c = \frac{f(S_+) - f(S_-)}{S_+ - S_-}. \tag{6}$$

This yields, respectively, for the convex case $c = 0.3$ and for the convex-concave case $c \approx 1.1538$. In Fig. 3 the red lines indicate these constant TW speeds. We observe that the adaptive moving mesh follows all waves very accurately.

3. THE TWO-DIMENSIONAL SITUATION

For the two-dimensional case of model (1) we make the following simplified choices for the fractional flow function f and diffusion function D:

$$f(S) = S^{\alpha}, \quad \mathcal{D}(S) = \beta S^{\alpha-\beta-1}, \quad \alpha > \beta + 1. \tag{7}$$

3.1. Non-Monotone Waves and Instabilities

In contrast with the 1D case, for which both the monotone and non-monotone waves are stable under small perturbations, the 2D model may give rise to *in*stabilities ("finger" structures). It can be shown that for specific values of $\tau > 0$, the non-monotone waves may become *un*stable. The analysis is based on the following observations, also mentioned in [15, 16].

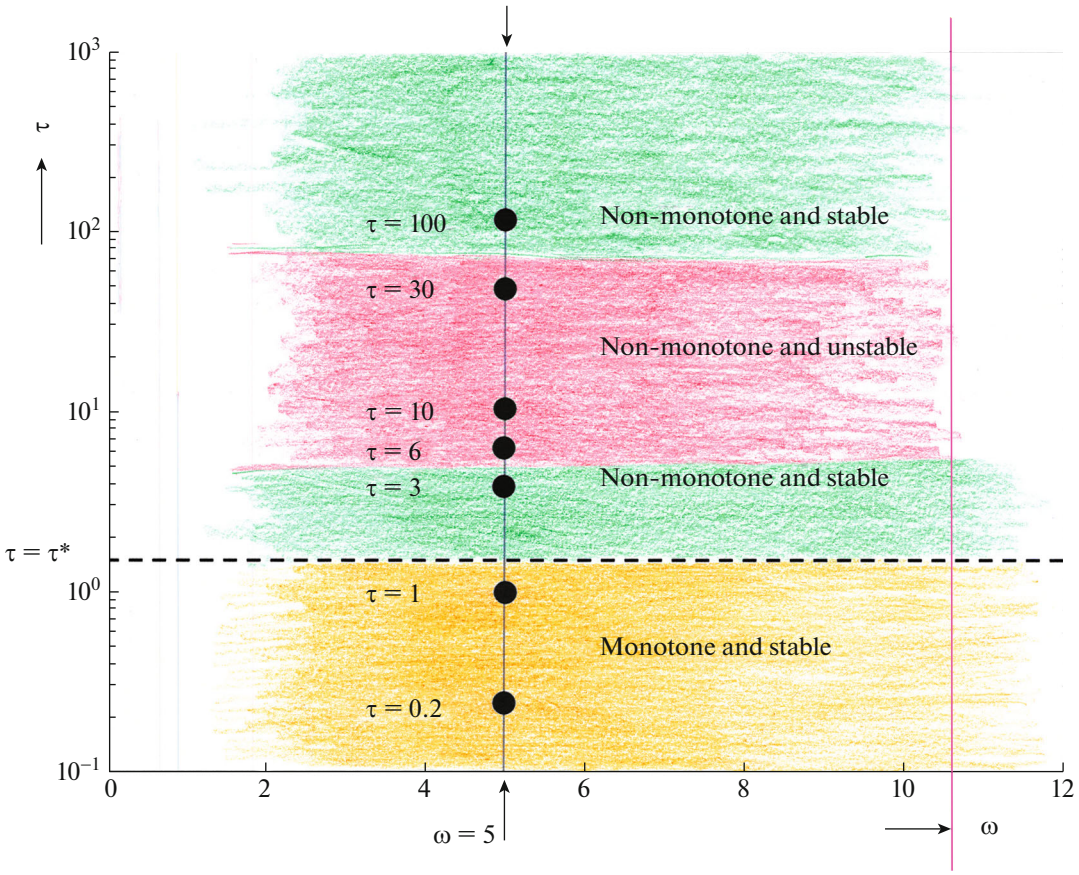

Fig. 6. An (ω, τ)-diagram that sketches the dependence of the stability and monotonicity properties of the PDE solution in two space dimensions. The seven black circles correspond with the seven numerical experiments in Figs. 7–10.

First, the non-equilibrium PDE (1) is rewritten as a system of two equations, one for the saturation S and one for the pressure p:

$$\begin{aligned} S_t &= \nabla \cdot (\mathcal{D}(S)\nabla p) + [f(S)]_z, \\ \tau S_t &= p - \mathcal{P}(S), \end{aligned} \tag{8}$$

where $\mathcal{P}(S)$ is an equilibrium pressure. Next, the PDEs are written in a travelling wave coordinate, similar as is done in Section 2.2.The saturation and pressure waves are then perturbed in the following form:

$$\begin{aligned} S &= S_0(\zeta) + \epsilon e^{i\omega_x + i\omega_z + kt} S_1(\zeta) + \mathbb{O}(\epsilon^2), \\ p &= p_0(\zeta) + \epsilon e^{i\omega_x + i\omega_z + kt} p_1(\zeta) + \mathbb{O}(\epsilon^2). \end{aligned} \tag{9}$$

These perturbed quantities are substituted in the system of two travelling wave equations, higher-order terms are being neglected, and equations for the linear stability analysis are set up. For these, it can be derived, that, for $\tau = 0$, the growth factor k will always be negative, whereas, for $\tau > 0$ and for certain frequencies ω, the growth factor can be positive, thereby initiating unstable waves. These can be related to so-called fingering structures, as we will see in Section 3.3.

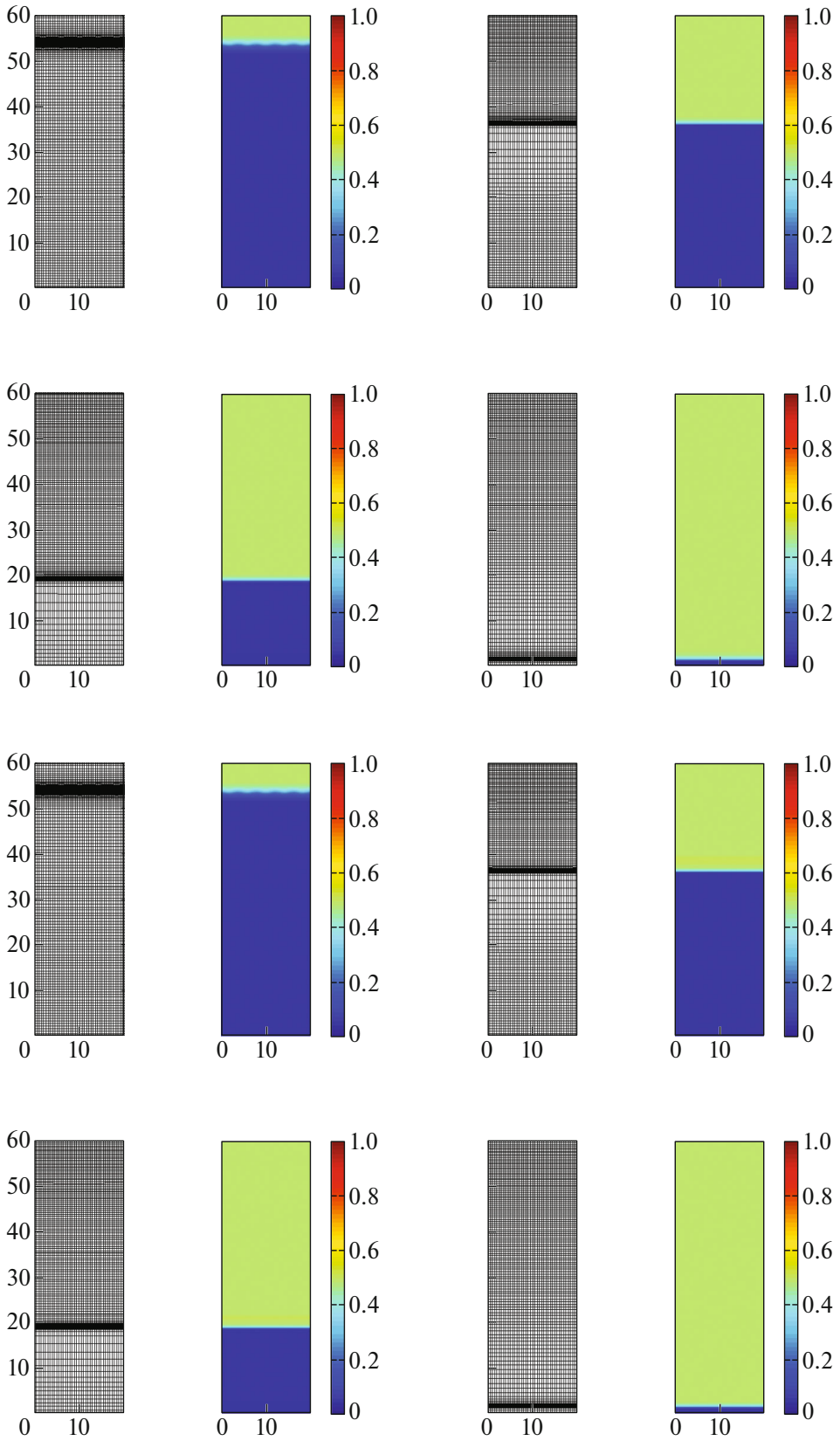

Fig. 7. The upper four plots for $t = 0,100,150,250$ show numerical results for the case $\tau = 0.2 < \tau_*$ (a monotone stable wave) and the lower four plots for $\tau = 1 < \tau^*$.

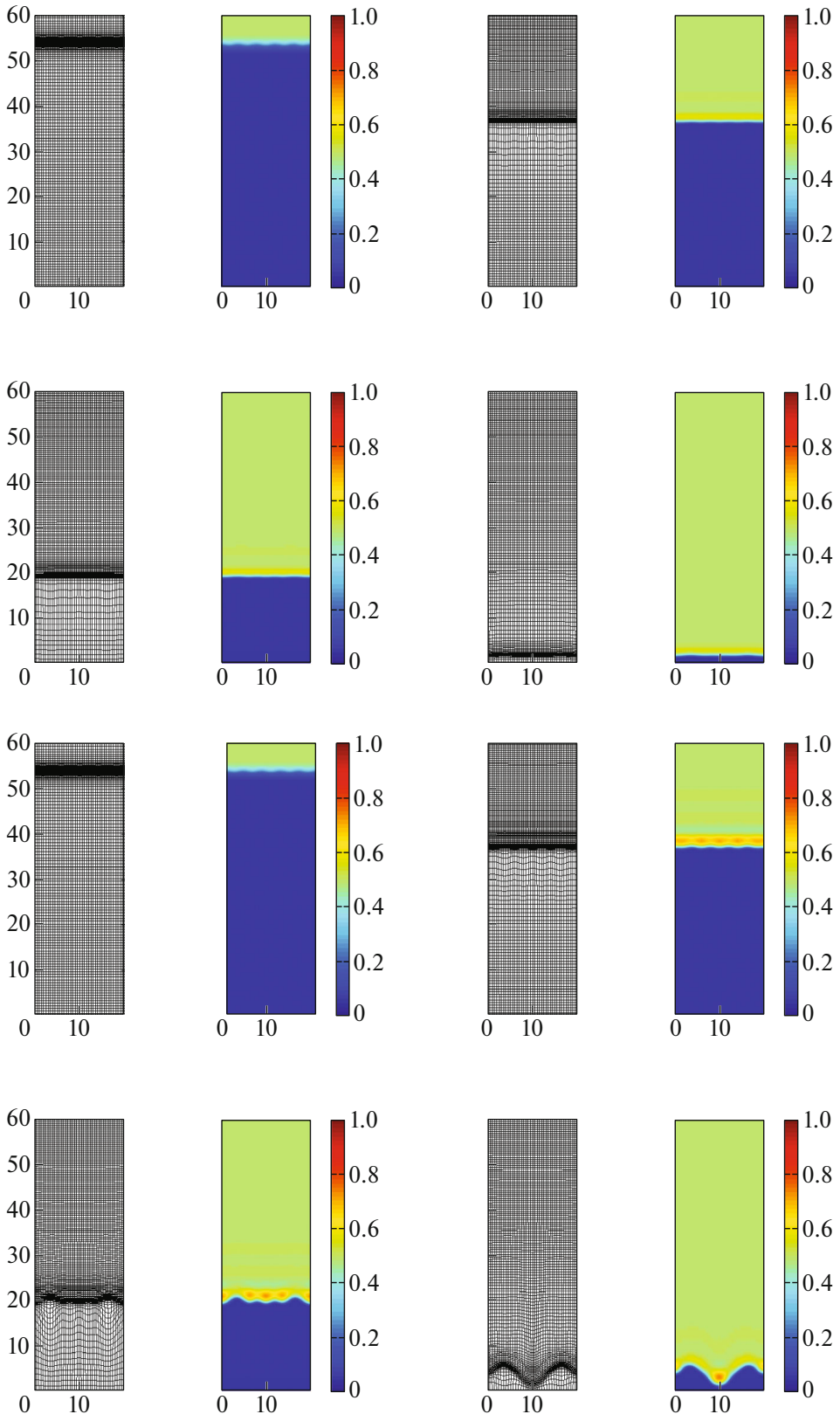

Fig. 8. The upper four plots for $t = 0,100,150,250$ show numerical results for the case $\tau = 3 > \tau_*$ (a non-monotone stable wave) and the lower four plots for $\tau = 6 > \tau_*$ (a non-monotone and unstable wave).

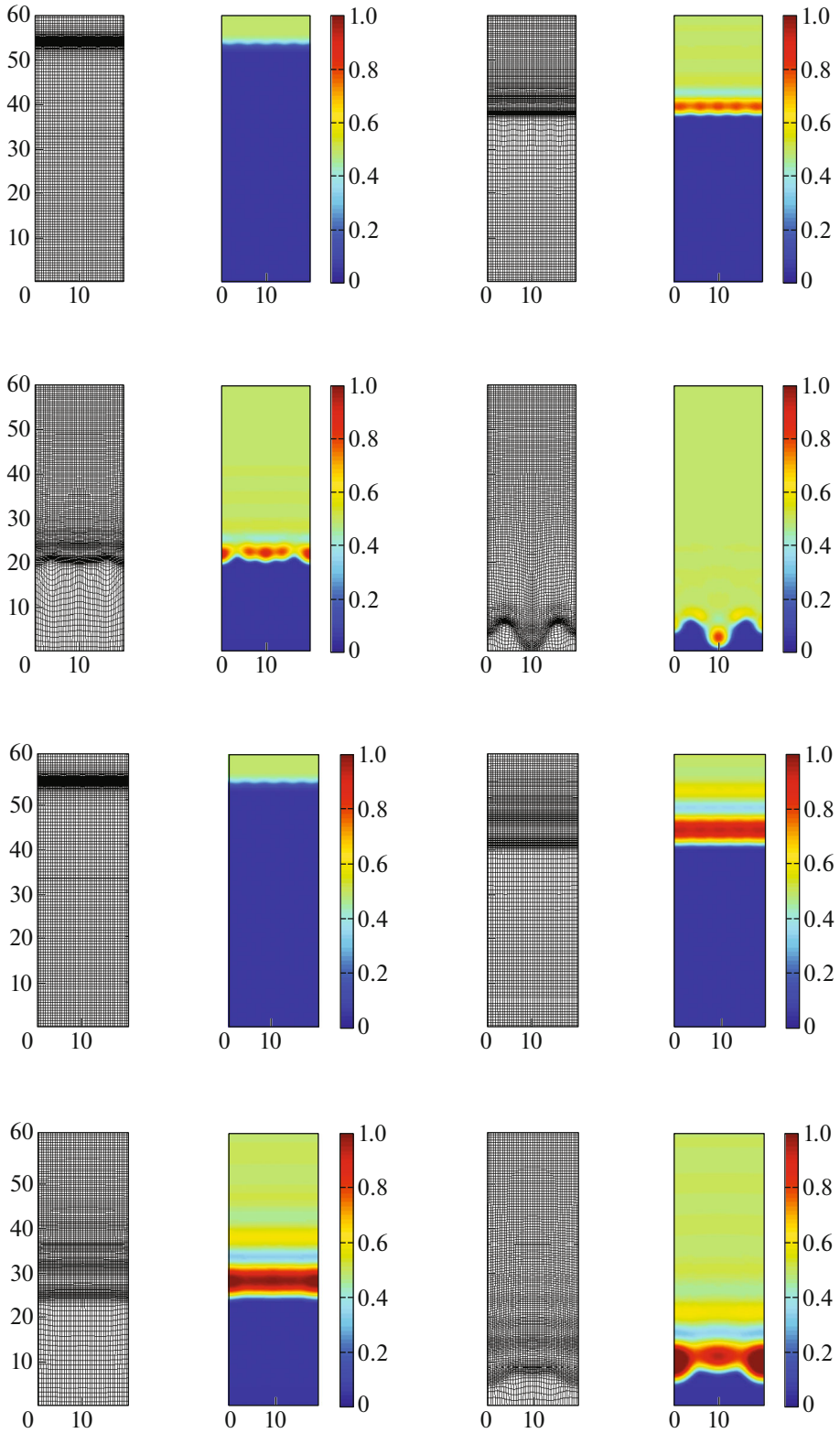

Fig. 9. The upper four plots for $t = 0,100,150,250$ show numerical results for the case $\tau = 10 > \tau_*$ and the lower four plots for $\tau = 30 > \tau_*$ (both non-monotone and unstable waves).

3.2. The Adaptive Moving Mesh in 2D

The adaptive mesh method in two dimensions follows similar principles, with some extra features and differences, compared to the 1D situation. More details can be found in, for example, [10, 11, 17–19]. Summarizing the procedure, the 2D mesh transformation reads:

$$\begin{aligned} x &= z(\xi,\eta,\vartheta),\\ z &= z(\xi,\eta,\vartheta),\\ t &= t(\xi,\eta,\vartheta) = \vartheta. \end{aligned} \tag{10}$$

Figure 4 (left panel) shows a typical 2D situation of transforming a steep PDE solution in the original coordinates to a milder one in the transformed coordinates. As an example, the first term of the nonlinear diffusion on the righthand side in PDE model (1) transforms to:

$$(\mathscr{D}(S)S_x)_x = \frac{1}{\mathscr{J}}\left[\left(\frac{\mathscr{D}(S)z_\eta^2}{\mathscr{J}}S_\xi\right)_\xi - \left(\frac{\mathscr{D}(S)z_\xi z_\eta}{\mathscr{J}}S_\eta\right)_\xi - \left(\frac{\mathscr{D}(S)z_\xi z_\eta}{\mathscr{J}}S_\xi\right)_\eta + \left(\frac{\mathscr{D}(S)z_\xi^2}{\mathscr{J}}S_\eta\right)_\eta\right], \tag{11}$$

where $\mathscr{J} = x_\xi z_\eta - x_\eta z_\xi$ denotes the determinant of the Jacobian of the two-dimensional transformation (10). The one-dimensional basic equidistribution principle, $[\mathscr{M}z_\xi]_\xi = 0$, is extended to a system of two coupled nonlinear elliptic PDEs:

$$\begin{aligned} &\nabla\cdot(\mathscr{M}\nabla x) = 0, \quad \nabla := \left[\frac{\partial}{\partial\xi},\frac{\partial}{\partial\eta}\right]^{\mathrm{T}},\\ &\nabla\cdot(\mathscr{M}\nabla z) = 0. \end{aligned}$$

where the monitor function $\mathscr{M}$ is now defined by

$$\mathscr{M} = \gamma(t) + \sqrt{\nabla S\cdot\nabla S}, \quad \text{with} \quad \gamma(t) = \iint\limits_{\Omega_c}\sqrt{\nabla S\cdot\nabla S}\,d\xi d\eta.$$

Figure 4 (right panel) describes the 2D adaptive mesh in terms of minimizing a "mesh-energy" functional and springs (connected mesh points) and forces (monitor values). It is obvious that more sophisticated monitor functions could be used, but, for the PDE model in this paper, this relatively simple monitor function has shown to be sufficiently effective. Note that we have added a time-dependent adaptivity function $\gamma(t)$ which is automatically calculated during the time-integration process. It provides additional smoothing to the mesh distribution and takes care of the scaling in the space and solution directions (see [17] for more information about this choice). It can be shown that the adaptive mesh transformation, following this 2D equidistribution principle with the mentioned monitor function $\mathscr{M}$, remains non-singular:

Theorem 1 (for details of the proof: [20]). *Let $\mathscr{M} > 0$, $\mathscr{M}\in C^1(\Omega_c)$ and $\mathscr{M}_\xi, \mathscr{M}_\eta \in C^\gamma(\bar\Omega_c)$ for $\gamma\in(0,1)$. Then there exists a unique solution $(x,z)\in C^2(\bar\Omega_c)$, which is a bijection from $\bar\Omega_c$ into itself. Moreover, the determinant of the Jacobian $\mathscr{J}$ satisfies*:

$$\mathscr{J} = x_\xi z_\eta - x_\eta z_\xi > 0.$$

Some important ingredients of their proof include the Jordan curve theorem, the Carleman–Hartman–Wintner theorem and the maximum principle for elliptic PDEs. In [21] a deep analysis of the invertibility of more general, so-called σ-harmonic, mappings is given. The transformed PDE model is spatially discretized uniformly in the ξ and η coordinates. For the numerical time-integration of the transformed 2D non-equilibrium PDE and the adaptive mesh equations, we have used an IMplicitEXplicit-approach [22, 23]. As an example, the diffusion term (11) is numerically approximated as follows:

$$\begin{aligned} (\mathscr{D}(S)S_x)_x\big|_{i,j}^n \approx \frac{1}{\mathscr{J}_{i,j}^n}\Bigg[&\frac{C_1|_{i+1,j}^n + C_1|_{i,j}^n}{2}\frac{S_{i+1,j}^{n+1} - S_{i,j}^{n+1}}{(\Delta\xi)^2} - \frac{C_1|_{i,j}^n + C_1|_{i-1,j}^n}{2}\frac{S_{i,j}^{n+1} - S_{i-1,j}^{n+1}}{(\Delta\xi)^2}\\ &- C_2|_{i+1,j}^n\frac{S_{i+1,j+1}^{n+1} - S_{i+1,j-1}^{n+1}}{4\Delta\xi\Delta\eta} + C_2|_{i-1,j}^n\frac{S_{i-1,j+1}^{n+1} - S_{i-1,j-1}^{n+1}}{4\Delta\xi\Delta\eta} - C_2|_{i,j+1}^n\frac{S_{i+1,j+1}^{n+1} - S_{i-1,j+1}^{n+1}}{4\Delta\xi\Delta\eta}\\ &+ C_2|_{i,j-1}^n\frac{S_{i+1,j-1}^{n+1} - S_{i-1,j-1}^{n+1}}{4\Delta\xi\Delta\eta} + \frac{C_3|_{i,j+1}^n + C_3|_{i,j}^n}{2}\frac{S_{i,j+1}^{n+1} - S_{i,j}^{n+1}}{(\Delta\eta)^2} - \frac{C_3|_{i,j}^n + C_3|_{i,j-1}^n}{2}\frac{S_{i,j}^{n+1} - S_{i,j-1}^{n+1}}{(\Delta\eta)^2}, \end{aligned} \tag{12}$$

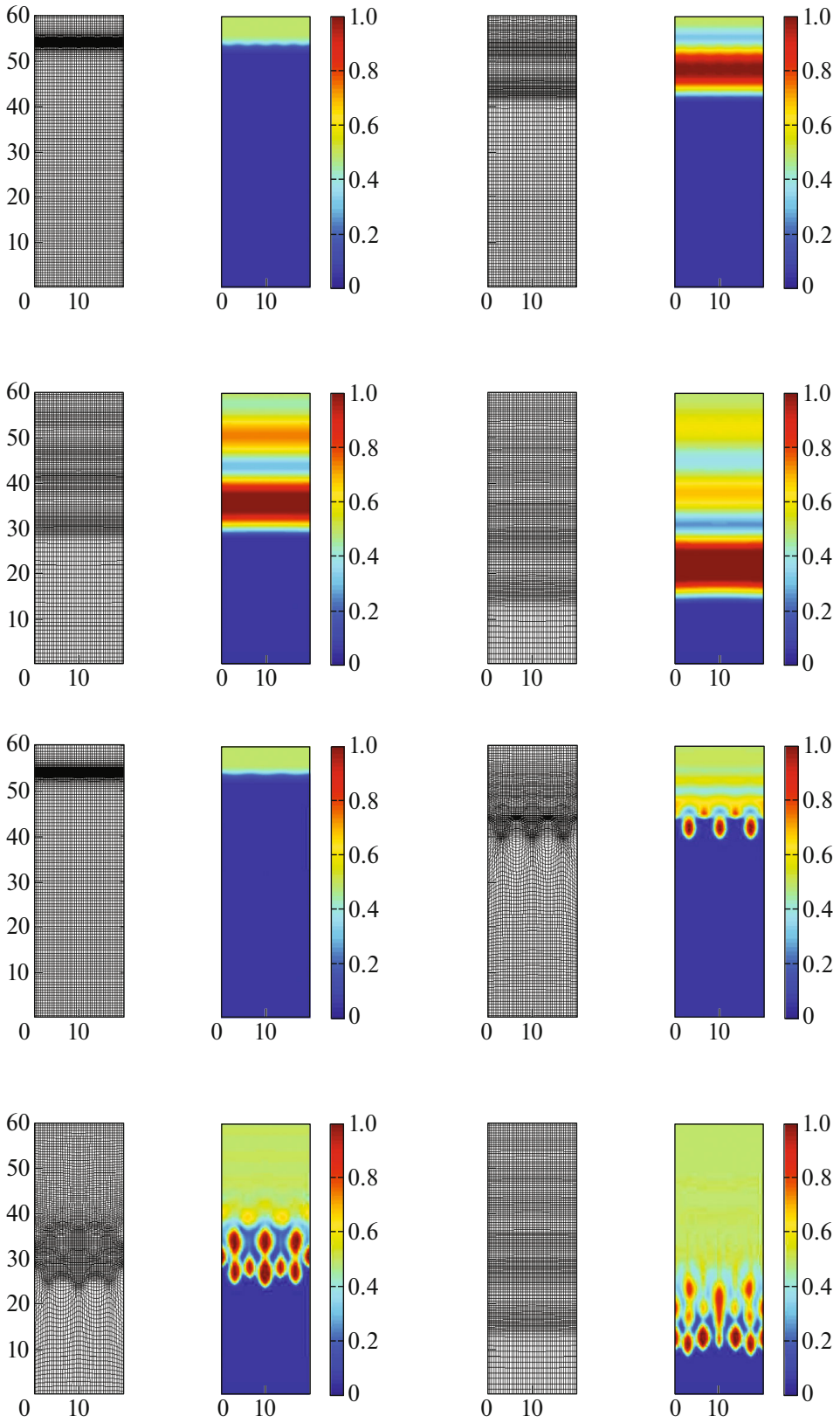

Fig. 10. The upper four plots for $t = 0,100,150,250$ show numerical results for the case $\tau = 100 \gg \tau_*$ (again a non-monotone stable wave!!) and the lower four plots for $\mathcal{D} = 0.1$ instead of $\mathcal{D} = 1$ (yielding an unstable structure in the form of "fingers").

where

$$C_1 := \frac{1}{\mathcal{J}}\mathcal{D}(S)z_\eta^2, \quad C_2 := \frac{1}{\mathcal{J}}\mathcal{D}(S)z_\xi z_\eta,$$

and

$$C_3 := \frac{1}{\mathcal{J}}\mathcal{D}(S)z_\xi^2,$$

respectively. Instead of the 'smart' smoothing operators in space and time, as being used in 1D, here, a filter, as in [18, 19], on the monitor function is applied several times in each time step in the following way:

$$\tilde{\mathcal{M}}_{i,j} = \frac{1}{4}\mathcal{M}_{i,j} + \frac{1}{8}[\mathcal{M}_{i-1,j} + \mathcal{M}_{i+1,j} + \mathcal{M}_{i,j-1} + \mathcal{M}_{i,j+1}]$$
$$+ \frac{1}{16}[\mathcal{M}_{i-1,j-1} + \mathcal{M}_{i+1,j-1} + \mathcal{M}_{i-1,j+1} + \mathcal{M}_{i+1,j+1}].$$

This modification yields even smoother mesh distributions and enhances the time-integration process as well.

3.3. Numerical Results

To confirm and support the theoretical predictions in the analysis in Section 3.1, we perform some numerical experiments for the 2D model. The spatial domain is defined by the rectangle $[0,10]\times[0,60]$ and the initial solution is a "tanh"-type function as in 1D, defined in Eq. (5), but now situated around the value 55. We add a small periodic perturbation with frequency ω to test the stability of the two-dimensional waves. The numerical experiments, unless specified differently, make use of a spatial mesh with 41×121 mesh points.

Figure 5 indeed confirms and illustrates the stability analysis by [15, 16], also briefly described in Section 3.1. The left panel shows the numerically calculated growth factor k of the perturbation as a function of the initial frequency ω for several values of the non-equilibrium parameter τ, using the adaptive mesh method from Section 3.2. The right panel is taken from [15] and depicts a very similar dependence of $k(\omega)$.

Figure 6 can be extracted from Fig. 5, if we create a diagram of the τ-dependence on the frequency ω. The seven black circles indicate the seven τ-values for $\omega = 5$ in the numerical experiments. For $\tau = 0.2$ and $\tau = 1$ a monotone and stable wave can be found as predicted: see Fig. 7. For $\tau = 3$ (upper four plots in Fig. 8) a non-monotone stable wave is produced. In the four lower plots of Fig. 8 we see, for $\tau = 6$, a *non*-monotone and *un*stable wave appearing. In Fig. 9, for $\tau = 10$ (upper four plots) and for $\tau = 30$ (lower four plots) we show more non-monotone and unstable waves. It can also be predicted, that for $\omega = 5$ and $\tau \gg 1$ (in this case $\tau = 100$), the non-monotone waves "become" stable again, because of an extra diffusion effect for higher values of the non-equilibrium parameter. This can be seen in Fig. 10 (upper four plots). Finally, in the lower four plots we have decreased the diffusion coefficient D from 1 to 0.1, thereby creating even more unstable structures in the form of "fingers". All runs have been performed with $\alpha = 3$, $\beta = 0.5$, a spatial mesh of 41×121 mesh points, 4000 time steps and a frequency $\omega = 5$ in the perturbed initial condition.

CONFLICT OF INTEREST

The author declares that he has no conflicts of interest.

REFERENCES

1. S. M. Hassanizadeh and W. G. Gray, "Thermodynamic basis of capillary pressure on porous media," Water Resour. Res. **29**, 3389–3405 (1993).
2. D. DiCarlo, "Experimental measurements of saturation overshoot on infiltration," Water Resour. Res. **40** (4), W04215 (2004).
3. M. J. Nicholl and R. J. Glass, "Infiltration into an analog fracture: Experimental observations of gravity-driven fingering," Vadose Zone J. **4**, 1123–1151 (2005).
4. C. Cuesta, C. J. van Duijn, and J. Hulshof, "Infiltration in porous media with dynamic capillary pressure: Travelling waves," Eur. J. Appl. Math. **11**, 381–397 (2000).

5. C. J. van Duijn, Y. Fan, L. A. Peletier, and I. S. Pop, "Travelling wave solutions for a degenerate pseudo-parabolic equation modelling two-phase flow in porous media," Nonlinear Anal. Real World Appl. **14**, 1361–1383 (2013).
6. C. J. van Duijn, S. M. Hassanizadeh, I. S. Pop, and P. A. Zegeling, "Non-equilibrium models for two-phase flow in porous media: The occurrence of saturation overshoot," *Proceedings of the 5th International Conference on Applications of Porous Media, Cluj-Napoca* (2013).
7. R. Hilfer, F. Doster, and P. A. Zegeling, "Nonmonotone saturation profiles for hydrostatic equilibrium in homogeneous porous media," Vadose Zone J. **11** (3), 201 (2012).
8. G. Hu and P. A. Zegeling, "Simulating finger phenomena in porous media with a moving finite element method," J. Comput. Phys. **230** (8), 3249–3263 (2011).
9. C. J. Budd, W. Huang, and R. D. Russell, "Adaptivity with moving grids," Acta Numer. **18**, 111–241 (2009).
10. A. van Dam and P. A. Zegeling, "A robust moving mesh finite volume method applied to 1D hyperbolic conservation laws from magnetohydrodynamics," J. Comput. Phys. **216**, 526–546 (2006).
11. W. Huang and R. D. Russell, "Analysis of moving mesh partial differential equations with spatial smoothing," SIAM J. Numer. Anal. **34**, 1106–1126 (1997).
12. P. A. Zegeling, I. Lagzi, and F. Izsak, "Transition of Liesegang precipitation systems: Simulations with an adaptive grid PDE method," Commun. Comput. Phys. **10** (4), 867–881 (2011).
13. P. A. Zegeling, *Adaptive Computations: Theory and Computation* (Science, Beijing, 2007), Chapter 7.
14. L. R. Petzold, "A description of DASSL: A differential/algebraic system solver," in *IMACS Transactions on Scientific Computation*, Ed. by R. S. Stepleman (1983), pp. 65–68.
15. A. G. Egorov, R. Z. Dautov, J. L. Nieber, and A. Y. Sheshukov, "Stability analysis of gravity-driven infiltrating flow," Water Resour. Res. **39**, 1266 (2003).
16. J. L. Nieber, R. Z. Dautov, A. G. Egorov, and A. Y. Sheshukov, "Dynamic capillary pressure mechanism for instability in gravity-driven flows; review and extension to very dry conditions," Transp. Porous Media **58**, 147–172 (2005).
17. A. van Dam and P. A. Zegeling, "Balanced monitoring of flow phenomena in moving mesh methods," Commun. Comput. Phys. **7**, 138–170 (2010).
18. T. Tang and H. Tang, "Adaptive mesh methods for one- and two-dimensional hyperbolic conservation laws," SIAM J. Numer. Anal. **41** (2), 487–515 (2003).
19. P. A. Zegeling, "On resistive MHD models with adaptive moving meshes," J. Sci. Comput. **24** (2), 263–284 (2005).
20. Ph. Clement, R. Hagmeijer, and G. Sweers, "On the invertibility of mappings arising in 2D grid generation problems," Numer. Math. **73** (1), 37–52 (1996).
21. G. Alessandrini and V. Nesi, "Univalent σ-harmonic mappings," Arch. Rational Mech. Anal. **158**, 155–171 (2001).
22. S. J. Ruuth, "Implicit-explicit methods for reaction–diffusion problems in pattern formation," J. Math. Biol. **34**, 148–176 (1995).
23. W. Hundsdorfer and J. Verwer, *Numerical Solution of Time-Dependent Advection–Diffusion–Reaction Equations* (Springer, Berlin, 1993).